ACS OMEGA

http://pubs.acs.org/journal/acsodf

Article

Enhanced Chitosan Photoluminescence by Incorporation of Lithium Perchlorate

Marlon Gurumendi, Floralba López, Luis J. Borrero-González, Thibault Terencio, Manuel Caetano, Carlos Reinoso, and Gema González*

Cite This: *ACS Omega* 2023, 8, 13763−13774

Read Online

ACCESS | Metrics & More | Article Recommendations | Supporting Information

ABSTRACT: An improvement in chitosan film photoluminescence was observed after adding $LiClO_4$. FTIR spectra, XPS, DFT calculations, and XRD measurements show an alteration of the H-bonds and an increase in the amorphous character of chitosan. PL spectra display a growth in intensity in the visible region along with the incorporation of lithium, signaling a possible rise in the population density of tail states and, consequently, better photon absorption, as observed from UV−vis measurements. A mechanism through aggregation-induced emission effect is proposed to explain the different results. Although this work establishes the relation between structural changes provoked by $LiClO_4$ incorporation and luminescence in the case of chitosan, we expect that the same approach could be generalized to similar polymeric structures.

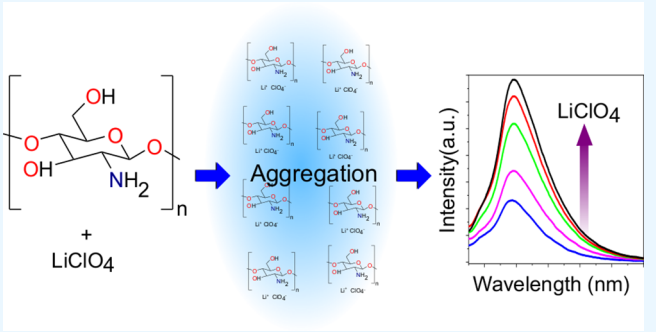

1. INTRODUCTION

Chitosan (CS) is a semicrystalline polysaccharide derived from chitin, the second most important natural polymer that can be extracted from the shells of crustaceans. Due to its physical and chemical properties, it has been an attractive alternative for several technological applications, including biomedical, pharmaceutical, and environmental applications.[1−9] CS has also been used extensively as a membrane matrix owing to its excellent film forming with good mechanical properties.[10,11] The structure comprises repeating units of N-acetyl D-glucosamine and D-glucosamine,[12] shown in Figure S1 in the Supporting Information.

Many hydroxyls and amine groups in polymers can act as electron donors,[2] facilitating the reactions with many organic and inorganic salts to form polyelectrolytes.[1,5,13−17] Adding salt to polymers causes changes in the structure, and in optical, electrical, and thermal properties.[1,14,18−20] In the case of chitosan, it provides ions as charge carriers that can improve the conductivity of the polymer, as has been reported in different works.[1,21,22] The most used dopants in the preparation of many polymer electrolytes are lithium salts like lithium perchlorate,[19,23,24] lithium tetraborate,[25] lithium hexafluorophosphate, and lithium trifluoromethanesulfonate.[26,27] Lithium salts are preferred due to their low interfacial strength and ability to coordinate and solvate easily, exhibiting their ionic conductivity character. The advantage of incorporating these salts is that a complexation can be obtained when the polymer electrolytes are prepared due to their high dissociation energy and good solubility in most solvents.[1]

The possibility of obtaining a biocompatible organic photoluminescent system is very attractive for bioimaging applications.[28−31] The photoluminescence properties of chitosan have attracted much attention due to its low toxicity and good biocompatibility, which offers applications as imaging probes. The photoluminescence of chitosan has been reported by some authors,[9,31−38] taking advantage of photoluminescence spectroscopy nondestructive nature.[39−41] Although, in general, fluorescence in macromolecules is caused by molecules with delocalized electrons at conjugated double bonds,[38,42] the CS oligomer featured a molecular structure that has no delocalized electrons. However, they have shown fluorescent properties.[32,38]

Some amino-containing polymers, such as chitosan, have been reported to present a photoluminescent effect.[9,32,36,43−46] CS has an emission band in the visible spectrum at 465 nm (with a laser excitation of 369 nm), attributed to its amine groups.[45] Furthermore, CS can be either stabilized or doped with luminescent agents,[32−34,38,46,47] adding optically active agents luminescent nanoparticles, such as quantum dots,[39,48,49] plasmonic nanoparticles (gold or silver),[6,50] organic complexes,[51−53] or polymeric nanoparticles.[54] CS's most common

Received: December 19, 2022
Accepted: March 16, 2023
Published: April 5, 2023

luminescent systems use lanthanide complexes, such as europium or terbium complexes, to get good luminescence properties for possible applications in electrochemical devices.[33,46,55]

The addition of lithium salts to CS has been studied mainly to improve ionic conductivity,[14,19,56,57] however, as far as we know, the photoluminescent effect of lithium salts in CS matrix has been scarcely reported. Therefore, looking for new hybrid biocompatible and environmentally friendly compounds with good film forming capability and high luminescence, chitosan with different amounts of $LiClO_4$ has been studied, which complement the well-known high ionic conductivity studies. In this work, experimental evidence is complemented for the first time with theoretical studies, and mechanisms that satisfy both observations are proposed to get new insight into the problem.

1.1. Methodology. *1.1.1. Materials.* CS flakes from shrimp shells (>75% deacetylation degree) were purchased from Sigma-Aldrich. Lithium perchlorate was received as a white crystalline salt from Sigma-Aldrich and acetic acid (glacial) 100% from Merck. Distilled water was used throughout the experiment, and all samples were prepared using the solution-casting technique.

1.1.2. Films Preparation. Chitosan solution 1% in acetic acid was prepared under magnetic stirring until the chitosan powder was completely dissolved. For pure chitosan film, the chitosan solution was stored in a plastic Petri dish and left to dry at room temperature. For hybrid films, lithium perchlorate salt was added to the chitosan solution to have 10, 25, 30, and 40% w/w in weight of lithium perchlorate salt concerning chitosan weight in the solution. After 15 min of stirring, the solution was poured into a plastic Petri dish and dried at room temperature for 3 days. The film thickness was measured using a digital micrometer with a precision 0.001 mm. The values obtained for each sample at different locations were averaged. Table S1 in Supporting Information summarizes the prepared hybrid compounds. For clarity and simplicity, the term $XLiClO_4$/CS will be used, where X refers to the composite percentage ratio of $LiClO_4$ weight relative to chitosan weight.

1.2. Structural and Morphological Characterization. *1.2.1. Scanning and Transmission Electron Microscopies.* The morphology of the samples was observed using a scanning electron microscope (SEM) FEI, INSPECT F50, and by transmission electron microscopy (TEM) with a Tecnai F20, operating at 200 kV. The samples were prepared by ultramicrotomy, using a Reichert FCS ultramicrotome with a cryo-sectioning accessory.

1.2.2. Fourier Transform Infrared Spectroscopy. The functional groups of chitosan hybrid films were characterized by Fourier transform infrared spectroscopy (FTIR). The spectrophotometer was a PerkinElmer model Spectrum 100, and the data of the samples were acquired in the absorbance mode at room temperature, in the range from 450 to 4500 cm^{-1}.

1.2.3. X-ray Diffractometry. The diffraction patterns of the samples were obtained with X-ray diffractometer PANalytical X'Pert Pro by using X'Pert High Source Plus and X'Pert Data Viewer programs. The equipment was operated using CuKα radiation source λ = 1.542 Å at 40 kV and 30 mA. The 2θ angles were scanned between 10° and 70°, with a step size of 0.1°. The degree of crystallinity (χ_c) of the polyelectrolyte was determined by using eq 1:[13,58]

$$\chi_C = \left[\frac{A_C}{(A_C + A_A)}\right] \times 100\% \quad (1)$$

where A_C and A_A are the areas of crystalline and amorphous peaks, respectively. The determination of amorphous and crystalline peaks was done by deconvolution of the peaks method. Baseline correction has been done before fitting multipeaks using the Gaussian function.

1.2.4. X-ray Photoelectron Spectroscopy. X-ray photoelectron spectroscopy surface analysis was performed on the pristine chitosan and also on each of the final materials having different percentages of lithium incorporated. For these measurements, a PHI VersaProbe III from Physical Scientific was used, equipped with a 180 hemispherical electron energy analyzer; using a monochromatized Al Kα source with energy 1486.6 eV operated with an energy band-pass 255 kV for the survey acquisition and 55 kV for high-resolution acquisition. Spot analysis had a diameter of 100 μm and the detection angle relative to the substrate surface was 45°. Analyses and fitting were performed using peak fit version 4.7 and Qtiplot version 0.9.8.9.

1.3. DFT Calculation. Density functional theory (DFT) calculations were conducted using the software Orca[59] on a representative glucosamine unit of the material alone and with Li^+ ion in different positions. The functional B3LYP[60,61] in conjunction with a Def2-TVZP (triple ζ) basis-set were used.[62,63] Dispersion interactions were included through Grimme approach DFT-D3 with Becke–Johnson damping (D3BJ).[64,65] All optimized structures were ensured to be minimal through the calculation of their frequencies. Calculations, including solvation, were done using an implicit CPCM model of water.[66] The simulated UV–vis spectra were generated using the TD-DFT method.

1.4. Optical Properties. *1.4.1. UV–Vis Spectroscopy.* UV–vis spectra of the composite films were collected in total transmittance mode using a UV/vis/NIR double beam spectrometer from PerkinElmer, model Lambda 1050, equipped with a 150 mm integration sphere accessory, in the wavelength range from 200 to 600 nm. Data analysis and visualization were performed using an application developed in R statistical programming language (https://github.com/mcaetanove/chemometrics.git). UV–vis spectra were smoothed by an adaptive-degree polynomial filter, using a maximum polynomial order of 4 and a data window of 11.[67]

The optical absorption for noncrystalline materials is commonly modeled by the Tauc and Davis-Mott equation,[68−70] given by

$$(\alpha h\nu) = \beta(h\nu - E_g)^{\gamma} \quad (2)$$

where $h\nu$ is the photon energy, h is Planck's constant, ν is the photon frequency, and α is the absorption coefficient. E_g is the energy bandgap (Tauc's bandgap), β is a constant that depends on the probability of transition, and γ is an index that describes the type of electronic transition which could be assumed to be 1/2 for allowed direct optical band gap or 2 for the allowed indirect optical band gap.[68−70]

The optical absorption coefficient α was calculated according to Lambert's Absorption Law:

$$\alpha(t) = \left(\frac{2.306}{t}\right) \times \text{Abs} \quad (3)$$

https://doi.org/10.1021/acsomega.2c08072
ACS Omega 2023, 8, 13763−13774

where Abs is the absorbance and t is the thickness of the sample.

1.4.2. Photoluminescence Spectroscopy. The photoluminescence (PL) spectra were recorded on a High-Resolution spectrometer HR4000CG−UV−NIR using the program Ocean Optics SpectraSuite. An excitation wavelength of 400 nm from a diode laser and an integration time of 5 s was used.

2. RESULTS AND DISCUSSION

2.1. Structural and Morphological Analysis.

2.1.1. XRD. The XRD patterns of the films of pure chitosan and chitosan loaded with different concentrations of $LiClO_4$ are presented in Figure 1. For pure chitosan, the diffractogram presents the characteristic diffraction peaks at 2θ 11.94° and 18.70°, assigned to intramolecular and intermolecular hydrogen bonds.[71] The films with different concentrations of $LiClO_4$, as can seen in Figure 1, show slight shifts in 2θ to lower angles from 11.94° to 11.87° and from 18.70° to 18.46°, respectively. Additionally, a decrease in the intensity of these peaks is observed as the $LiClO_4$ concentration increases. The halo in the 2θ region between 15° and 30° becomes broader, especially for the case of the sample with 40$LiClO_4$/CS, suggesting an increase in the amorphous structure of chitosan.[13,72] The broadening, shifting, and lowering of the relative intensity of chitosan diffraction peaks with the incorporation of $LiClO_4$ can be attributed to the complexation of $LiClO_4$ in the polymer chains, occurring between the functional groups of chitosan and the ions of the dopant salt,[27,73,74] resulting in an increase amorphization with the increasing addition of $LiClO_4$. The above agrees with previous studies on chitosan doped with different salts that reported an increase in amorphization with the addition of salts.[13,19,27,74−76]

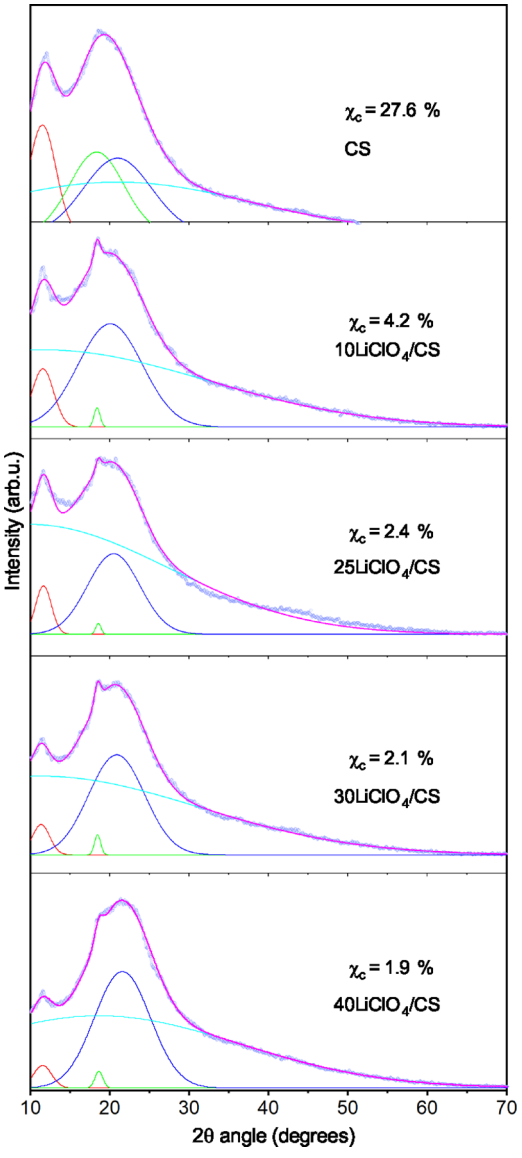

Figure 1. Diffractogram of different prepared films among the respective deconvolution to evaluate the crystallinity of different prepared films.

The degree of crystallinity, denoted by χ_c, of the prepared films was determined by eq 1 are indicated in each diffractogram in Figure 1, suggesting that the amorphousness of the poly electrolyte films increased with the salt concentration. The initial chitosan sample (without lithium) had a higher crystallinity percentage, ∼28%, progressively decreasing to a value of ∼2% for the sample with the highest salt concentration.

2.1.2. SEM and TEM. The morphology of chitosan thin film with different concentrations of $LiClO_4$ is presented in the SEM images, taken in electron backscattered mode (Figure 2(a−f)). The image of the pure chitosan film, presented in Figure 2(a), shows a smooth and homogeneous nonporous structure. As the $LiClO_4$ concentration increases, the matrix shows the formation of a second phase.

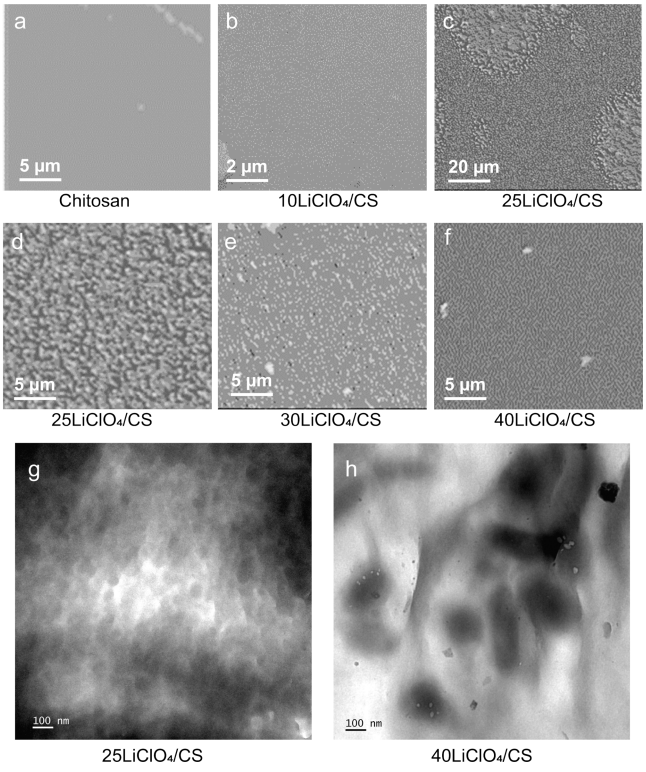

Figure 2. SEM micrographs of different prepared films. Samples (a) pure chitosan, (b) 10$LiClO_4$/CS, (c) and (d) 25$LiClO_4$/CS, (e) 30$LiClO_4$/CS, (f) 40$LiClO_4$/CS. TEM micrographs of different prepared films (g) 25$LiClO_4$/CS and (h) 40$LiClO_4$/CS.

https://doi.org/10.1021/acsomega.2c08072
ACS Omega 2023, 8, 13763−13774

For 10$LiClO_4$/CS film, small clusters (<10 nm) with a very uniform distribution are presented in Figure 2(b). For 25$LiClO_4$/CS the formation of some spherulites[77] can be seen at low magnification (Figure 2(c)), while at high magnification (Figure 2(d)) a higher density of the small clusters between 50 and 100 nm can be identified, clearly seen by TEM micrographs presented in Figure 2(g). For 30$LiClO_4$/CS film, similar-sized aggregates are present (Figure 2(e)). For 40$LiClO_4$/CS, a higher density of clusters whose sizes are in the range of 200−400 nm can be identified in Figure 2(f), which is also seen by TEM (Figure 2(h)). It seems that for low $LiClO_4$ concentration, the acid polysaccharide molecules from CS react with the ionic species forming small aggregates of less than 10 nm (Figure 2(b)) as the $LiClO_4$ concentration increases the aggregate size and density. The resulting structures might be stabilized as the local supersaturation increases, forming nanoclusters with size in the range of 50−400 nm, as can be seen in Figure 2(g,h). Similar cluster sizes have been reported for different authors.[53,78]

2.1.3. FT-IR. FT-IR studies were conducted to follow the chemical modifications in chitosan structure upon interaction with $LiClO_4$ (Figure 3). The chitosan film spectrum (Figure 3(a)) shows a broad band centered at 3475 cm^{-1} assigned to the stretching vibration of the hydroxyl group; the presence of the broadband at 3244 cm^{-1} is attributed to the N−H stretching.[79] The absorbance band at 2907 cm^{-1} is associated with C−H symmetric and asymmetric stretching. The peak at 1652 cm^{-1} is assigned to the C═O stretching in NH−CO−CH_3 group (amide I).[79] The pH of the precursor suspension of the film constrains the protonation degree of NH group, for pH < 6.5 protonation is favored with the corresponding bending vibrations of the protonated amine group appearing at 1550 cm^{-1}, while the N−H band in the amide group (amide II) appears at a higher frequency around 1560 cm^{-1}.[79]

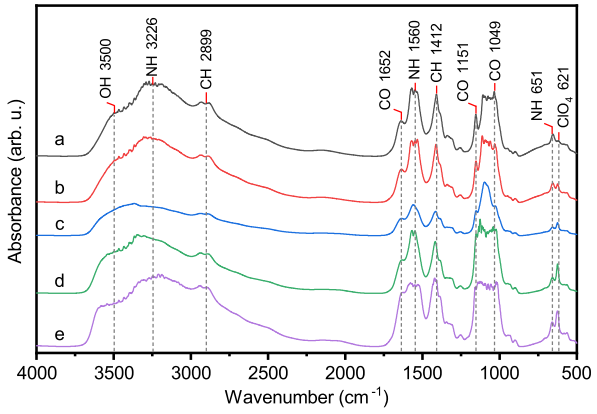

Figure 3. FTIR spectra of (a) pure chitosan, (b) 10$LiClO_4$/CS, (c) 25$LiClO_4$/CS, (d) 30$LiClO_4$/CS, and (e) 40$LiClO_4$/CS.

The stretching vibration of C−H, CH_2, and CH_3 groups are observed at 1412 cm^{-1} and around 1375 cm^{-1}. The peak at 1151 cm^{-1} corresponds to the C−O−C bridge asymmetric stretching mode.[79,80] The signals in the region around 1080−1025 cm^{-1} correspond to the stretching vibration of C−O−H, C−O−C, and CH_2−O−H present in the pyranose ring. The peak observed at 665 cm^{-1} is ascribed to the N−H twist vibration. Table S2 shown in Supporting Information presents the FTIR peak assignments of chitosan. The different X$LiClO_4$/CS FTIR spectra (Figure 3(b−e)) show all the main signals of pure chitosan, although some shifts with respect to pure chitosan can be observed. In the chitosan spectrum, the O−H stretching resonance band is significantly broad and centered at 3500 cm^{-1}, clearly signaling the presence of intramolecular hydrogen bonds.[81]

To gain more insight into the structural features, the second spectra derivative was taken applying the Norris-Williams Derivative Filter (5 smoothing points and five differential gaps).[82] This procedure enriches the qualitative interpretation of the FTIR results and provides a basis to discuss the effect of $LiClO_4$ interaction with chitosan moieties. Figure 4(a,b) shows the second derivative of the FTIR spectra at 3700−3500 cm^{-1} and 1590−1500 cm^{-1}, respectively, for CS and X$LiClO_4$/CS.

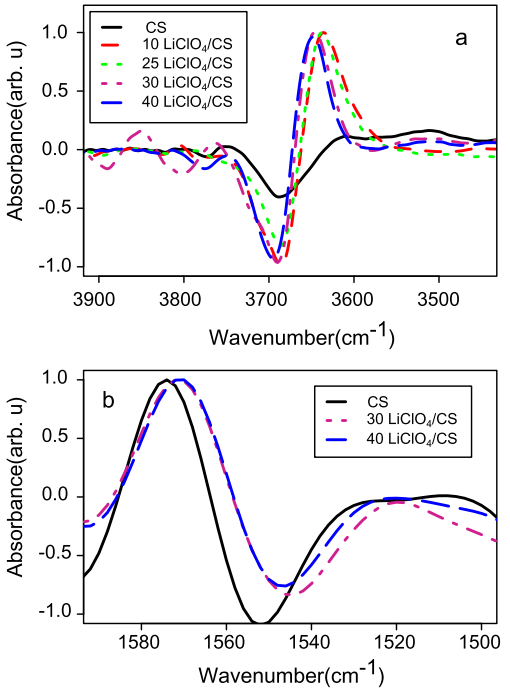

Figure 4. (a) Second derivative of 3900−3500 cm^{-1} and (b) 1590−1500 cm^{-1} spectral regions for different concentrations of $LiClO_4$.

In the presence of $LiClO_4$ a new absorption band appears around 3640 cm^{-1} in the O−H stretching region. The blue-shifting of this band was accentuated as the $LiClO_4$ concentration increased, which seems to suggest an interaction of Li^+ ions with the OH^- of chitosan. This interaction may lead to hydroxyl groups being released from the hydrogen-bond network, the O−H bond length decreases, the constant force increases, and the frequency suffers a blue-shift.[81] In addition, the presence of $LiClO_4$ causes a shift of the band associated with the N−H bending of amine to lower wavenumbers to the pure chitosan, as can be seen in Figure 4(b). This may be associated with Li^+ and ClO_4^- ions binding to the amine groups.[19,57,76]

2.1.4. XPS. The survey spectra of 40$LiClO_4$/CS and chitosan films are presented in Figure 5(a) and (b), respectively, exhibiting clear features at 56 eV (Li 1s) and 199 eV (Cl 2p) confirming the presence of lithium and chlorine, respectively.[35,83−88] A magnification of this eV region is presented in the inset of Figure 5(a), so the Li 1s peak at 56 eV can be seen. In contrast, in the inset in Figure 5(b), showing the same eV region but for pure chitosan, this peak is not present, as expected.

https://doi.org/10.1021/acsomega.2c08072
ACS Omega 2023, 8, 13763−13774

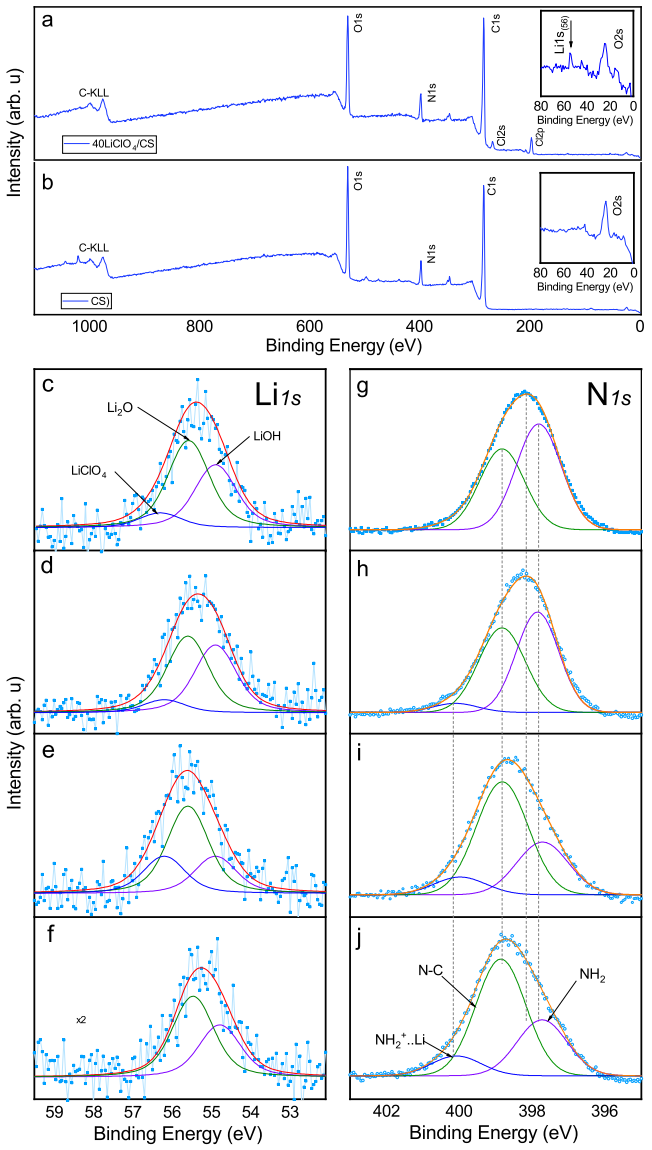

Figure 5. XPS survey spectra of prepared films, (a) 40$LiClO_4$/CS and (b) pure chitosan. XPS spectra of Li 1s core levels: (c) 40%, (d) 30%, (e) 25%, and (f) 10% of w/w $LiClO_4$/CS films; and N 1s core levels: (g) CS, (h) 10%, (i) 30%, and (j) 40% of w/w $LiClO_4$/CS films. A decrease of counts of NH_2 at 397.9 eV is shown while an increasing signal at 400.2 eV by the incorporation of lithium in the sample is seen.

Different concentrations for the lithium chemical environment are revealed with an improved resolution and displayed in Figure 5(c–f), where a deconvolution process of the four samples is presented. The fitting was performed without background subtraction, using a Voigt adjustment. An error of ±0.2 eV is due to the data dispersion and to XPS resolution ~0.5 eV. The high resolution spectra recordings lead to finding LiOH, Li_2O, and $LiClO_4$ at 54.9, 55.6, and 56.4 eV (±0.2 eV), respectively, indicated in Figure 5(c).[85−87] The XPS cross-section for lithium is quite small, the reason the counts are very low; however, the XPS technique is able to detect low contributions of lithium.[35] The scale of intensity of spectrum for sample 10$LiClO_4$/CS (Figure 5(f)), has been enlarged twice (2×) for a better visualization. The presence of lithium compounds formed by combination with oxygen and chlorine confirms the existence of lithium in the different samples in different concentrations. Table 1 presents the comparative contributions of each lithium compound in each sample. This suggests an ionic exchange between chitosan electron charge and lithium perchlorate.

Table 1. Chemical Environment Contribution of Lithium Dispersed in Chitosan from Fitting XPS Spectra

	Lithium species detected		
Sample	LiOH (at.%)	Li_2O (at.%)	$LiClO_4$ (at.%)
CS	-	-	-
10$LiClO_4$/CS	39.5	60.45	<0.1
25$LiClO_4$/CS	23.15	53.69	<0.1
30$LiClO_4$/CS	43.1	48.39	8.28
40$LiClO_4$/CS	38.4	52.60	8.98

The N 1s core level (Figure 5(g–j)) exhibits a clear interaction between the NH_2 and the lithium, whose presence shifts the binding energy from 397.9 to 400.2 eV that appears in correspondence with the concentration raised of lithium in the sample. This suggests the formation of species $-NH_2-Li^+$ with higher energy bonding. At the same time the binding energy assigned to the −N−C− interaction at 398.8 eV remains almost constant in agreement with the molecular stability of chitosan.[89,90]

2.2. DFT Calculations. Chitosan is composed of alternating units of β-(1−4)-D-glucosamine and *N*-acetyl-D-glucosamine. The ratio between one and the other depends on the degree of acetylation, which can be tuned through the preparation medium used. With this consideration in mind, theoretical calculations were conducted on one glucosamine unit[91] considering three different models possible: (i) the protonated form NH_3, (ii) the normal glucosamine form NH_2, and (iii) the acetylated form. Using the IR spectrum for each form, the most stable chair conformer and boat conformer were calculated, and they are shown in Figure S2 in the Supporting Information. The comparison with experimental FTIR spectra allows concluding which form is present in the evaluated material. It should be noted that the experimental spectra are much more complex than the theoretical ones as each unit constituting the chitosan could be in a different form, different conformation, and linked to another unit in a different manner.

As expected, the spectra of the three different forms display similar features: a very intense band at 1050 cm^{-1}, two around 3000 cm^{-1}, and two bands at 1450 and 1520 cm^{-1}. However, the acetylated form presents an intense band at 1700 cm^{-1} characteristic of C═O stretching. This particular feature does not seem to appear in the experimental spectrum suggesting few units are present in the acetylated form. For NH_2 and NH_3 forms, it is difficult to judge which one is more abundant only from the IR spectrum as both present very similar features. However, by careful inspection, the NH_2 form seems more abundant, most notably by the presence of the N−H twist band at 650 cm^{-1}. While the calculations do not take into account solvent effects such as hydrogen bonding with solvent molecules, and hence the calculated N−H and O−H are considerably shifted, it seems that the broadband at higher wavenumber in the experimental spectrum does not correspond only to the different glucosamine forms. This discrepancy could be explained due to the experimental procedure where some water can also be present in the final material. In order to probe this hypothesis, a lone water

https://doi.org/10.1021/acsomega.2c08072
ACS Omega 2023, 8, 13763−13774

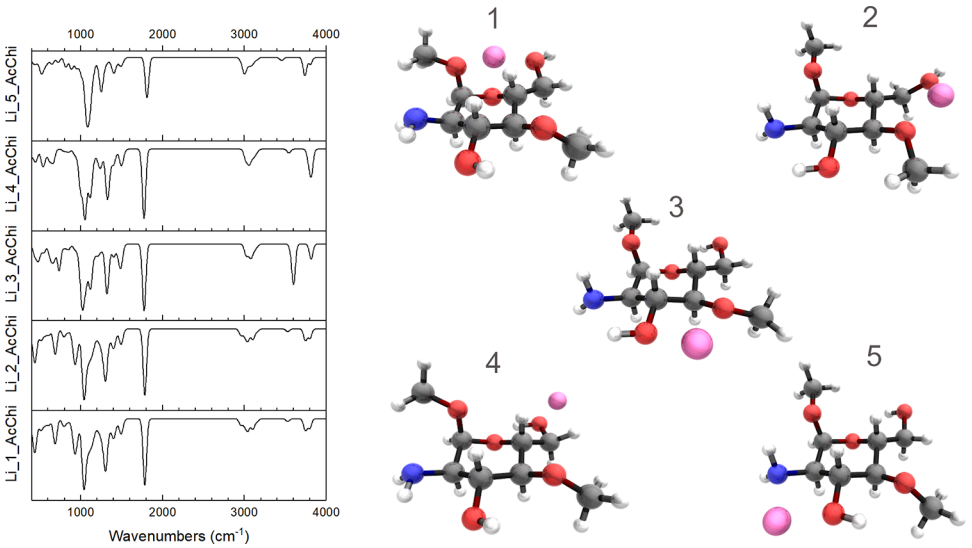

Figure 6. Structures of glucosamine with different location sites for lithium and their associated simulated IR-spectra. Atom colors — O: red, N: blue, C: gray, H: white, Li: pink.

molecule, a glucosamine unit with one or two water molecules with explicit and implicit solvation mimicking water was simulated.

Water molecules normally possess 3 normal vibrations modes: O−H stretching symmetric, O−H stretching asymmetric, and H−O−H bending. The water molecules were placed close to the oxygen and nitrogen of the glucosamine unit allowing H-bonding. Spectra calculated for NH_2 forming glucosamine units with these water molecules in different locations are shown in Figure S3 in Supporting Information, displaying a broad band in the higher region, confirming the aforementioned hypothesis. The shift observed between the experimental and calculated frequency for O−H stretching of water is due to the model being limited to only one or two water molecules and the calculation method, but it is well-known that the frequency corresponding to this vibration should be at lower wavenumbers.

Five different structures, varying the location sites of lithium adsorption on CS, and considering glucosamine units in the NH_2 form, are depicted in Figure 6. In position 1, lithium interacts with three oxygen atoms. In positions 2 and 4, the lithium ion only interacts with one hydroxyl group. Position 3 involves the interaction with both hydroxyl and methyl groups, while in position 5 the lithium ion is positioned between nitrogen and oxygen atoms. Each different structure was optimized, and the frequencies calculated all positives, to ensure minimum energy structures were obtained. One remark is that all optimizations lead to positions close to groups that are more electronegative, e.g., N and O atoms. Logically, this can be explained by considering that Li^+ establish electrostatic interactions with the partial negative charge in the chitosan.

In the five location sites of lithium considered, there are three different kinds of groups interacting with Li ion: C−OH, NH_2, and C−O−C. Two regions are affected by the change of position of lithium ion, one low region between 400 and 800 cm^{-1} and the upper region between 3000 and 4000 cm^{-1}. This observation is corroborated by the experimental results where most changes occur also in these regions. In fact, the higher region seems to be more affected by the lithium presence. The positions where the most changes are observed in this region are positions 3 and 4; a very intense band appears at 3460 and 3000 cm^{-1}, respectively. Interestingly, this band corresponds to the O−H stretching in both cases where the lithium is close to this group. However, lithium is also close to an OH group in position 1, but this very intense band is not observed. The main difference between position 1 and position 4 is that the group OH is involved in an intramolecular H-bond in the latter. By the comparison between theoretical and experimental results, we can affirm that lithium is close to groups OH establishing H-bonds and particularly affecting it.

There is a clear interplay between lithium position and H-bonds. In our calculations, only one unit of glucosamine was considered and we observe only intramolecular H-bond, but this effect would probably be the same in the case of intermolecular H-bonds. Lithium ions could play a role in forming the aggregates with chitosan, and probably in the luminescence, not only through electrostatic interaction but also by affecting the H-bonds. Figure 6 shows simulated IR spectra of species with lithium in different positions on the boat form of acetylated species.

Energetically, positions 2 and 5 were found to be the most stable; with a difference of only 4 kJ/mol in favor of position 5. Positions 3 and 1 are less stable than positions 5 by 14 and 17 kJ/mol, respectively. Position 4 is clearly less stable with a difference of 115 kJ/mol higher, highlighting a clear preference of the Li^+ for more than one neighboring electronegative atom. The exact same tendency is observed when considering Gibbs energies shown in section 3 of Supporting Information (Tables S3 and S4). However, the experimental spectrum presents very broad bands in this region and renders it impossible to conclude the exact location of lithium ion and is probably a combination of the most stable positions, namely, 5 and 2. When considering an implicit solvent model position 5 is clearly more stable than all the other positions (by at least 20 kJ/mol).

Finally, we simulated the different lithium species which could be formed: $LiClO_4$, LiOH, Li_2O, and Li_2CO_3. Although the comparison with the experimental spectra does not permit us to conclude unequivocally on the presence of one or several of these species, the XPS experimental results showed mainly the presence of LiOH, Li_2O associated with the groups N and OH from chitosan. Section 4 of the Supporting Information

https://doi.org/10.1021/acsomega.2c08072
ACS Omega 2023, 8, 13763−13774

shows the calculated IR spectra for these lithium species (Figure S4).

2.3. Optical Properties. *2.3.1. UV−vis Spectroscopy.* The UV−vis absorbance spectra of chitosan films containing 0, 10, 25, 30, and 40% w/w $LiClO_4$/CS are shown in Figure 7(a).

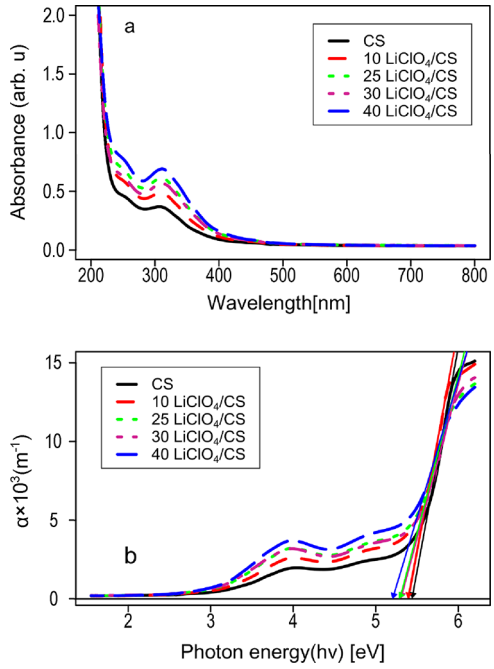

Figure 7. (a) UV−vis absorbance spectra of $XLiClO_4$/CS and (b) optical absorption coefficients of pure and loaded CS samples as a function of photon energy.

The spectra show two relatively broad absorption bands centered at ca. 250 and 310 nm, which are associated with the $n - \pi^*$ and $\pi - \pi^*$ transitions of the conjugated ring system.[49,92−94] A positive correlation between optical absorption intensity and incorporation of $LiClO_4$, as well as a minimal bathochromic shift (redshift) ≈ 4 nm, is observed, related to light scattering from Li^+/CS aggregates; this is in agreement with SEM and TEM observations. Figure 7(b) represents the optical absorption coefficients of pure and loaded chitosan samples as a function of photon energy.

Table 2 shows the absorption edge values determined by extrapolating the linear portion of the spectra to a zero

Table 2. Estimated Absorption Edges and Optical Bandgaps from $XLiClO_4$/CS Composite Films

Sample	Absorption Edge [eV][a]	$E_{g,d}$ [eV][a] $\gamma = 1/2$	$E_{g,i}$ [eV][a] $\gamma = 2$
CS	5.46	5.66	5.19
$10LiClO_4$/CS	5.41	5.62	4.99
$30LiClO_4$/CS	5.31	5.60	4.85
$40LiClO_4$/CS	5.20	5.51	4.75

[a]Standard Deviation = 0.01.

absorption value from the spectra shown in Figure 7(b). The absorption edge of the chitosan films slightly shifts toward the lower photon energy as the $LiClO_4$ concentration in the chitosan matrix increases.

The optical absorption for noncrystalline materials is commonly modeled by the Tauc and Davis-Mott equation. Although polymeric materials have highly complicated electronic structures Tauc models could be applicable.[95,96] The fluctuation of the polymeric lattice configuration blurs the fundamental edge and causes the presence of an Urbach tail. Also, the formation of solutions produces discrete energy levels in the bandgap, which will be reflected in the absorption coefficient.

Allowed direct and indirect transition energies, $E_{g,d}$ and $E_{g,i}$, were obtained from both $(\alpha h\nu)^2$ vs $h\nu$ (photon energy) and $(\alpha h\nu)^{1/2}$ vs $h\nu$ plots, respectively, and by extrapolating the linear parts of the curves until they intersect on the x-axis (zero absorption), as shown in Figure 8. For pure chitosan, direct and indirect bands lie at 5.66 and 5.19 eV, respectively, while for $XLiClO_4$/CS doped films, the values are given in Table 2.

From Table 2, it can be seen that the band edge and both direct and indirect band gaps decrease with increasing $LiClO_4$ concentration. It would be expected that the incorporation of $LiClO_4$ does not alter the chitosan band gap drastically, only some shifts in the bands attributable to electron−hole interaction between valence and conduction band were observed.

2.3.2. PL Spectroscopy. The photoluminescence (PL) spectra recorded at room temperature of chitosan and chitosan with different $LiClO_4$/CS percentages (10, 25, 30 and 40%w/w) are shown in Figure 9(A). All spectra show a broad emission band in the visible range. With the incorporation of the salt, the integrated area increases linearly with the subsequent loading (see inset in Figure 9(A)), where the sample loaded with 40% has an integrated area of about 3 times the integrated area of the sample of pure chitosan.

The increase in emission intensity with the incorporation of $LiClO_4$ can be attributed to the ability of chitosan to chelate metal ions due to its amino and hydroxyl groups. The complexation between chitosan and $LiClO_4$ has been demonstrated by FTIR, XPS, and DFT calculations, where a shift of the N−H vibrations was observed, and the enhancement of the vibration band located at 1144 cm^{-1} and of the band at 1067 cm^{-1}, suggests complexation with $Li^+ClO_4^-$ and the interaction of the amino groups of chitosan with these species.

A deconvolution was performed to the PL spectra (Figure S5 in the Supporting Information), and based on the peak positions of the fits, an energy band diagram was constructed for the evaluated system; see Figure 9(B). After optical excitation at 400 nm (3.10 eV) within tail states[70,97,98] below the conduction band, the excitation relaxes via nonradiative processes until finding luminescent centers with a subsequent relaxation to tail states above the valence band. These luminescent centers are related to defect states and are located in the intervals 436−444 nm (2.84−2.79 eV), 491−494 nm (2.52−2.50 eV), and 528−536 nm (2.35−2.31 eV).

The luminescence mechanism could be explained by aggregation-induced emission (AIE) phenomena, where aggregate formation can restrict the intramolecular motions turning on luminescence. The latter can effectively dissipate exciton energy and the radiative transition is activated. TEM analysis (Figure 2) shows the formation of dark clusters in the polymer matrix, with an average size of 50 nm for the composite film $25LiClO_4$/CS and in the range of 120−300 nm for $40LiClO_4$/CS. Therefore, the larger the cluster the higher the luminescence intensity (Figure 9(A)). On aggregation, the molecules become rigidified, this kind of luminescence is

https://doi.org/10.1021/acsomega.2c08072
ACS Omega 2023, 8, 13763−13774

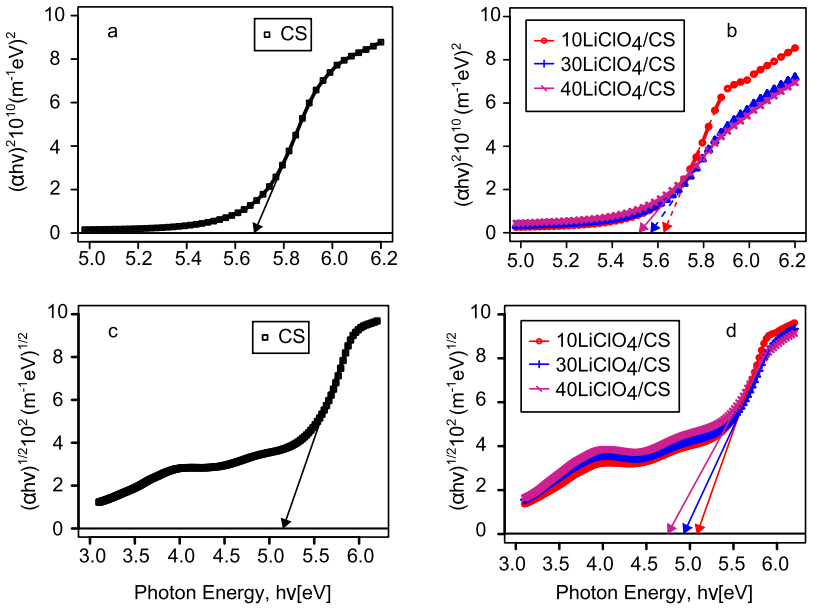

Figure 8. Tauc plot for allowed direct—(a) pure chitosan and (b) composite films (10, 30, 40)$LiClO_4$/CS—and indirect—(c) pure chitosan and (d) composite films X$LiClO_4$/CS—transitions.

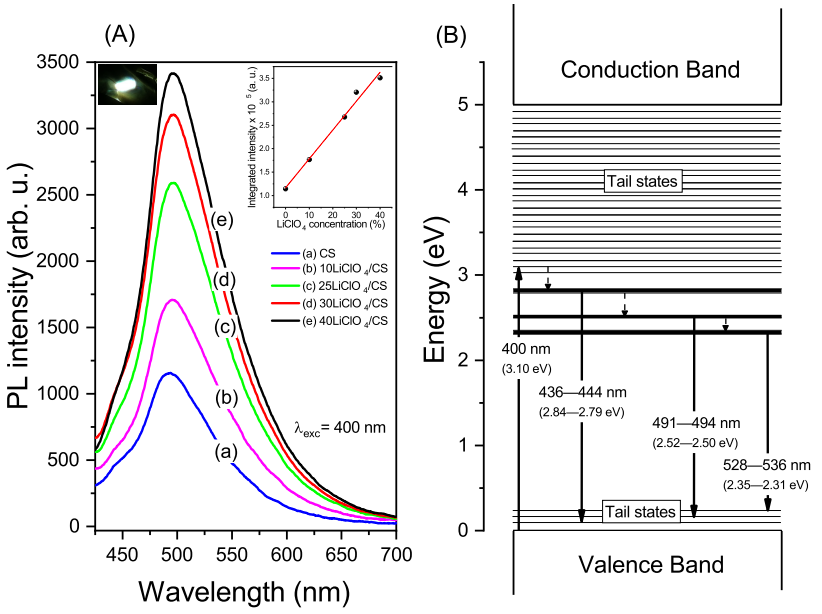

Figure 9. (A) Photoluminescence spectra for different samples of the evaluated films. On the upper left side, a photograph of one of the tested samples when it is being irradiated is shown. On the upper right side, the increasing linear trend of the integrated area can be observed with different percentages of $LiClO_4$. (B) Band diagram.

known as rigidification-induced emission (RIE) and has been observed in different natural polymers.[99,100]

On the other hand, the increase in the amorphization character observed by XRD (Figure 1) with the addition of $LiClO_4$ is associated with the increase of inter- and intramolecular charge transfer transitions between lithium ions and the amine and OH groups of chitosan via stretching vibration.[1] Amorphization and cluster formation cause suppression of molecular motions in the glassy matrix, and a rigidification of luminogenic molecules occurs. A similar photoluminescence mechanism has been reported in cotton fibers.[101] With the addition of $LiClO_4$ to chitosan, there are numerous electron-rich heteroatoms with lone-pair electrons in their molecular structures. The rigidified conformation during cluster formation can become highly luminescent by forming clustoluminogens since the aggregation promotes intra- and intermolecular interaction with the Li^+ and ClO_4^- ions.

Figure 9(B) shows the band diagram associated with the transitions observed during the PL of the different samples. The distributions of conduction, valence, and electronic states in chitosan do not end abruptly at the band edges. Instead, due to defects (amorphous material), some localized states, called tail states, appear deep in the gap region. Defects in chitosan come from dangling bonds, holes, pores, ruptures, and other macroscopic defects. The increase in PL emission with the $LiClO_4$ concentration could be attributed to the weakening of

https://doi.org/10.1021/acsomega.2c08072
ACS Omega 2023, 8, 13763−13774

hydrogen bonds, increasing the amorphization (defects), and, consequently, the density of tail states. IR spectra, XRD, and theoretical calculations support the above.

Furthermore, it can be seen that the wavelength of the emission peak for the chitosan sample is 493.58 nm, and with the incorporation of the $LiClO_4$ the peak wavelength increases to 496.16 nm, which corresponds to a peak wavelength shift on the order of 2.6 nm. This shift can be due to a compression of the emitting energy levels of chitosan due to the formation of aggregates.

3. CONCLUSIONS

The incorporation of $LiClO_4$ affects the structure and, consequently, the optical properties of chitosan, as there is a strong interplay between both phenomena. The complexation between chitosan and Li^+ has been demonstrated by FTIR, XPS, and DFT calculations, where the specificity of Li^+ for more electronegative atoms (O and N) was deduced. Moreover, DFT calculations and IR results show that the presence of Li^+ in the close vicinity of an H-bond would influence the O−H and N−H stretching and, subsequently, the strength of the H-bonds. Since the crystalline structure of chitosan strongly depends on the inter- and intramolecular hydrogen bonds between the OH and NH_2 groups, introducing Li^+ would logically affect its crystallinity. Indeed, an increase in the amorphization character of the hybrid material, along with the addition of $LiClO_4$, is observed from XRD results.

Concerning the optical properties, the absorption and emission of light have been observed to increase with the incorporation of lithium. While the optical band gap is large for chitosan, small transitions can be observed at energy differences inferior to the band gap due to the presence of tail states. Incorporating lithium, the decrease in crystallinity generates structural defects, which would increase the number of these tail states. Apart from the tail states, the intensity corresponding to each absorption band in UV−vis increase with $LiClO_4$ incorporation. The increase can be explained by the aggregation of polymeric parts around Li^+, increasing the local concentration of absorbing groups and allowing the polymeric material to absorb more photons, which permits, in turn, display of higher luminescence. The promising results of optical properties open new possibilities in tailoring the design of molecules. The route used in this work could be generalized to different polymers bearing electronegative atoms such as N or O: introducing lithium to form local aggregates resulting in improved UV−vis photon absorption and, thus, its luminescence.

■ ASSOCIATED CONTENT

Supporting Information

The Supporting Information is available free of charge at https://pubs.acs.org/doi/10.1021/acsomega.2c08072.

Additonal experimental details (PDF)

■ AUTHOR INFORMATION

Corresponding Author

Gema González − *Yachay Tech University, School of Physical Sciences and Nanotechnology, Urcuquí 100119, Ecuador; Centro de Ingenieria de Materiales y Nanotecnologia, Instituto Venezolano de Investigaciones Cientificas, Caracas 1020A, Venezuela;* orcid.org/0000-0003-4526-2429; Email: ggonzalez@yachaytech.edu.ec

Authors

Marlon Gurumendi − *Yachay Tech University, School of Physical Sciences and Nanotechnology, Urcuquí 100119, Ecuador*

Floralba López − *Yachay Tech University, School of Chemical Sciences and Engineering, Urcuquí 100119, Ecuador*

Luis J. Borrero-González − *Pontificia Universidad Católica del Ecuador, Facultad de Ciencias Exactas y Naturales, Escuela de Ciencias Físicas y Matemática, Laboratorio de Óptica Aplicada, Quito 17-01-2184, Ecuador;* orcid.org/0000-0003-3853-5433

Thibault Terencio − *Yachay Tech University, School of Chemical Sciences and Engineering, Urcuquí 100119, Ecuador*

Manuel Caetano − *Yachay Tech University, School of Chemical Sciences and Engineering, Urcuquí 100119, Ecuador; Universidad Central de Venezuela, Facultad de Ciencias, Escuela de Química, Caracas 1020A, Venezuela;* orcid.org/0000-0002-8891-3140

Carlos Reinoso − *Yachay Tech University, School of Physical Sciences and Nanotechnology, Urcuquí 100119, Ecuador*

Complete contact information is available at: https://pubs.acs.org/10.1021/acsomega.2c08072

Notes

The authors declare no competing financial interest.

■ ACKNOWLEDGMENTS

This work employed the Imbabura cluster of Yachay Tech University, which was purchased under contract No. 2017-024 (SIE-UITEY-007-2017). The authors would like to acknowledge the internal grants CHEM19-15 and Proyecto 6: "Estudio teórico de los efectos geométricos del ámbito cercano de los enlaces hidrógenos y su efecto en la interacción con la luz" of Yachay Tech University for supporting this work and providing the facilities required to carry out this work, as well as to Professor César Costa (Escuela Politécnica Nacional in Ecuador), for his collaboration with the photoluminescence measurements.

■ REFERENCES

(1) Aziz, S. B.; Woo, T. J.; Kadir, M.; Ahmed, H. M. A conceptual review on polymer electrolytes and ion transport models. *Journal of Science: Advanced Materials and Devices* **2018**, *3*, 1−17.

(2) Khiar, A.; Puteh, R.; Arof, A. Conductivity studies of a chitosan-based polymer electrolyte. *Physica B: Condensed Matter* **2006**, *373*, 23−27.

(3) Wang, J.; Chen, C. Chitosan-based biosorbents: modification and application for biosorption of heavy metals and radionuclides. *Bioresource technology* **2014**, *160*, 129−141.

(4) Motelica, L.; Ficai, D.; Ficai, A.; Truşcă, R.; Ilie, C.; Oprea, O.; Andronescu, E. Innovative antimicrobial chitosan/ZnO/Ag NPs/citronella essential oil nanocomposite—potential coating for grapes. *Foods.* **2020**, *9* (12), 1801−1827.

(5) Turco, B. O.; Boni, F. I.; Gremião, M. P. D.; Chorilli, M. Nanostructured polyelectrolyte complexes based on chitosan and sodium alginate containing rifampicin for the potential treatment of tuberculosis. *Drug Dev. Ind. Pharm.* **2021**, *47*, 1904−1914.

(6) Nakal-Chidiac, A.; Garcíta, O.; García-Fernández, L.; Martín-Saavedra, F. M.; Sánchez-Casanova, S.; Escudero-Duch, C.; San Roáman, J.; Vilaboa, N.; Aguilar, M. R. Chitosan-stabilized silver

nanoclusters with luminescent, photothermal and antibacterial properties. *Carbohydr. Polym.* **2020**, *250*, 116973.
(7) Rasool, B.; Zubair, M.; Khan, M. A.; Ramzani, P. M. A.; Dradrach, A.; Turan, V.; Iqbal, M.; Khan, S. A.; Tauqeer, H. M.; Farhad, M.; et al. Synergetic efficacy of amending Pb-polluted soil with P-loaded jujube (Ziziphus mauritiana) twigs biochar and foliar chitosan application for reducing Pb distribution in moringa leaf extract and improving its anti-cancer potential. *Water, Air, & Soil Pollution* **2022**, *233*, 344.
(8) Abourehab, M. A.; Pramanik, S.; Abdelgawad, M. A.; Abualsoud, B. M.; Kadi, A.; Ansari, M. J.; Deepak, A. Recent advances of chitosan formulations in biomedical applications. *International journal of molecular sciences* **2022**, *23*, 10975.
(9) Lv, S.; Liang, S.; Zuo, J.; Zhang, S.; Wei, D. Preparation and application of chitosanbased fluorescent probes. *Analyst* **2022**, *147*, 4657−4673.
(10) Wan, Y.; Creber, K. A.; Peppley, B.; Bui, V. T. Chitosan-based electrolyte composite membranes: II. Mechanical properties and ionic conductivity. *J. Membr. Sci.* **2006**, *284*, 331−338.
(11) Aziz, S. B.; Woo, T. J.; Kadir, M.; Ahmed, H. M. A Short Review on Chitosan Membrane for Biomolecules Immobilization. *J. Membr. Sci.* **2015**, *9*, 1−8.
(12) Rinaudo, M. Chitin and chitosan: Properties and applications. *Prog. Polym. Sci.* **2006**, *31*, 603−632.
(13) Aziz, S. B.; Abdullah, O. G.; Rasheed, M. A.; Ahmed, H. M. Effect of high salt concentration (HSC) on structural, morphological, and electrical characteristics of chitosan based solid polymer electrolytes. *Polymers* **2017**, *9*, 187.
(14) Aziz, S. B.; Abidin, Z. H. Z. Role of Hard-Acid/Hard-Base Interaction on Structural and Dielectric Behavior of Solid Polymer Electrolytes Based on Chitosan-XCF_3SO_3 (X= Li). *Journal of Polymers* **2014**, *2014*, 1.
(15) Ahmad, M.; Ahmed, S.; Swami, B. L.; Ikram, S. Adsorption of heavy metal ions: role of chitosan and cellulose for water treatment. *Langmuir* **2015**, *79*, 109−155.
(16) Urbaniak, T.; García-Briones, G. S.; Zhigunov, A.; Hladysh, S.; Adrian, E.; Lobaz, V.; Krunclová, T.; Janousková, O.; Pop-Georgievski, O.; Kubies, D. Quaternized Chitosan/ Heparin Polyelectrolyte Multilayer Films for Protein Delivery. *Biomacromolecules* **2022**, *23*, 4734−4748.
(17) Ferreira, D. C. M.; Ferreira, S. O.; de Alvarenga, E. S.; Soares, N. d. F. F.; dos Reis Coimbra, J. S.; de Oliveira, E. B. Polyelectrolyte complexes (PECs) obtained from chitosan and carboxymethylcellulose: A physicochemical and microstructural study. *Carbohydrate Polymer Technologies and Applications* **2022**, *3*, 100197.
(18) Aziz, S. B.; Abdullah, O. G.; Hussein, S. A. Role of silver salts lattice energy on conductivity drops in chitosan based solid electrolyte: Structural, morphological and electrical characteristics. *J. Electron. Mater.* **2018**, *47*, 3800−3808.
(19) Saravanan, A.; Ramasamy, R. P. Chitosan-maghemite-LiClO 4−a new green conducting superpara magnetic nanocomposite. *Journal of Polymer Research* **2016**, *23*, 1−11.
(20) KK, R.; Jang, W.; Kim, S.; Kim, T.-H. Chitosan-grafted-Gallic Acid as a Nature- Inspired Multifunctional Binder for High-Performance Silicon Anodes in Lithium-Ion Batteries. *ACS Appl. Energy Mater.* **2022**, *5*, 3166−3178.
(21) Ngai, K. S.; Ramesh, S.; Ramesh, K.; Juan, J. C. A review of polymer electrolytes: fundamental, approaches and applications. *Ionics* **2016**, *22*, 1259−1279.
(22) Shukur, M.; Ithnin, R.; Kadir, M. Electrical properties of proton conducting solid biopolymer electrolytes based on starch−chitosan blend. *Ionics* **2014**, *20*, 977−999.
(23) Fauzi, I.; Arcana, I.; Wahyuningrum, D. Synthesis and characterization of solid polymer electrolyte from N-succinyl chitosan and lithium perchlorate. *Advanced Materials Research.* **2014**, *896*, 58−61.
(24) Perumal, P.; Selvin, P. C.; Selvasekarapandian, S.; Sivaraj, P.; Abhilash, K.; Moniha, V.; Devi, R. M. Plasticizer incorporated, novel eco-friendly bio-polymer based solid bio-membrane for electrochemical clean energy applications. *Polym. Degrad. Stab.* **2019**, *159*, 43−53.
(25) Ramesh, S.; Yin, T. S.; Liew, C.-W. Effect of dibutyl phthalate as plasticizer on high-molecular weight poly (vinyl chloride)−lithium tetraborate-based solid polymer electrolytes. *Ionics* **2011**, *17*, 705−713.
(26) Liew, C.-W.; Ramesh, S.; Ramesh, K.; Arof, A. Preparation and characterization of lithium ion conducting ionic liquid-based biodegradable corn starch polymer electrolytes. *J. Solid State Electrochem.* **2012**, *16*, 1869−1875.
(27) Wang, A.; Tu, Y.; Wang, S.; Zhang, H.; Yu, F.; Chen, Y.; Li, D. A PEGylated Chitosan as Gel Polymer Electrolyte for Lithium Ion Batteries. *Polymers* **2022**, *14*, 4552.
(28) Li, K.; Wang, X.; Tong, A. A "turn-on" fluorescent chemosensor for zinc ion with facile synthesis and application in live cell imaging. *Analytica chimica acta* **2013**, *776*, 69−73.
(29) Bian, P.; Zhou, J.; Liu, Y.; Ma, Z. One-step fabrication of intense red fluorescent gold nanoclusters and their application in cancer cell imaging. *Nanoscale* **2013**, *5*, 6161−6166.
(30) Xie, G.; Ma, C.; Zhang, X.; Liu, H.; Yang, L.; Li, Y.; Wang, K.; Wei, Y. Chitosan-based cross-linked fluorescent polymer containing aggregation-induced emission fluorogen for cell imaging. *Dyes Pigm.* **2017**, *143*, 276−283.
(31) Xu, Q.; Ren, M.; Liu, K.; Wang, X.; Wang, J.-Y.; Wang, S.; Kong, F. Construction of chitosan-based fluorescent probe for real-time monitoring of viscosity changes in living cells with low cytotoxicity and high photostability. *Chem. Eng. J.* **2022**, *430*, 132851.
(32) Marpu, S. B.; Benton, E. N. Shining light on chitosan: A review on the usage of chitosan for photonics and nanomaterials research. *International journal of molecular sciences* **2018**, *19*, 1795.
(33) Tsvirko, M.; Mandowska, E.; Biernacka, M.; Tkaczyk, S.; Mandowski, A. Luminescence properties of chitosan doped with europium complex. *J. Lumin.* **2013**, *143*, 128−131.
(34) Saeed, S. E.-S.; El-Molla, M. M.; Hassan, M. L.; Bakir, E.; Abdel-Mottaleb, M. M.; Abdel-Mottaleb, M. S. Novel chitosan-ZnO based nanocomposites as luminescent tags for cellulosic materials. *Carbohydr. Polym.* **2014**, *99*, 817−824.
(35) Watts, J. F.; Wolstenholme, J. *An introduction to surface analysis by XPS and AES*; John Wiley & Sons, 2019.
(36) Pan, X.; Ren, W.; Gu, L.; Wang, G.; Liu, Y. Photoluminescence from Chitosan for Bio-Imaging. Australian. *J. Chem.* **2014**, *67*, 1422−1426.
(37) Huang, H.; Liu, F.; Chen, S.; Zhao, Q.; Liao, B.; Long, Y.; Zeng, Y.; Xia, X. Enhanced fluorescence of chitosan based on size change of micelles and application to directly selective detecting Fe3+ in humanserum. *Biosens. Bioelectron.* **2013**, *42*, 539−544.
(38) Lee, H. M.; Kim, M. H.; Yoon, Y. I.; Park, W. H. Fluorescent Property of Chitosan Oligomer and Its Application as a Metal Ion Sensor. *Marine Drugs* **2017**, *15*, 105.
(39) Zhao, H.; Liu, G.; You, S.; Camargo, F. V.; Zavelani-Rossi, M.; Wang, X.; Sun, C.; Liu, B.; Zhang, Y.; Han, G.; et al. Gram-scale synthesis of carbon quantum dots with a large Stokes shift for the fabrication of eco-friendly and high-efficiency luminescent solar concentrators. *Energy Environ. Sci.* **2021**, *14*, 396−406.
(40) Zhao, H.; Benetti, D.; Tong, X.; Zhang, H.; Zhou, Y.; Liu, G.; Ma, D.; Sun, S.; Wang, Z. M.; Wang, Y.; et al. Efficient and stable tandem luminescent solar concentrators based on carbon dots and perovskite quantum dots. *Nano Energy* **2018**, *50*, 756−765.
(41) Zhao, H.; Sun, R.; Wang, Z.; Fu, K.; Hu, X.; Zhang, Y. Zero-Dimensional Perovskite Nanocrystals for Efficient Luminescent Solar Concentrators. *Adv. Funct. Mater.* **2019**, *29*, 1902262.
(42) Sauer, M.; Hofkens, J.; Enderlein, J. *Handbook of fluorescence spectroscopy and imaging: from ensemble to single molecules*; John Wiley & Sons, 2010.
(43) Magesh, G.; Bhoopathi, G.; Nithya, N.; Arun, A.; Kumar, E. R. Tuning effect of polysaccharide Chitosan on structural, morphological, optical and photoluminescence properties of ZnO nanoparticles. *Superlattices Microstruct.* **2018**, *117*, 36−45.

https://doi.org/10.1021/acsomega.2c08072
ACS Omega 2023, 8, 13763−13774

(44) Greenham, N. C.; Peng, X.; Alivisatos, A. P. Charge separation and transport in conjugated-polymer/semiconductor-nanocrystal composites studied by photoluminescence quenching and photoconductivity. *Phys. Rev. B* **1996**, *54*, 17628−17637.
(45) Pan, X.; Wang, G.; Lay, C. L.; Tan, B. H.; He, C.; Liu, Y. Photoluminescence from amino-containing polymer in the presence of CO2: Carbamato anion formed as a fluorophore. *Sci. Rep.* **2013**, *3*, 1−6.
(46) Zhang, B.; Dong, X.; Zhou, Q.; Lu, S.; Zhang, X.; Liao, Y.; Yang, Y.; Wang, H. Carboxymethyl chitosan−promoted luminescence of lanthanide metallogel and its application in assay of multiple metal ions. *Carbohydr. Polym.* **2021**, *263*, 117986.
(47) Alves, R.; Sentanin, F.; Sabadini, R.; Pawlicka, A.; Silva, M. M. Green polymer electrolytes of chitosan doped with erbium triflate. *J. Non-Cryst. Solids* **2018**, *482*, 183−191.
(48) Nie, Q.; Tan, W. B.; Zhang, Y. Synthesis and characterization of monodisperse chitosan nanoparticles with embedded quantum dots. *Nanotechnology* **2006**, *17*, 140.
(49) Wu, Q.; Zhang, S.; Li, S.; Yan, Y.; Yu, S.; Zhao, R.; Huang, L. Chitosan-based carbon dots with multi-color-emissive tunable fluorescence and visible light catalytic enhancement properties. *Nano Research* **2022**, 1−11.
(50) Duan, Y.; Duan, R.; Liu, R.; Guan, M.; Chen, W.; Ma, J.; Chen, M.; Du, B.; Zhang, Q. Chitosan-stabilized self-assembled fluorescent gold nanoclusters for cell imaging and biodistribution in vivo. *ACS Biomater. Sci. Eng.* **2018**, *4*, 1055−1063.
(51) Berger, J.; Reist, M.; Mayer, J. M.; Felt, O.; Peppas, N.; Gurny, R. Structure and interactions in covalently and ionically crosslinked chitosan hydrogels for biomedical applications. *Eur. J. Pharm. Biopharm.* **2004**, *57*, 19−34.
(52) Liu, A.; Song, H.; Jia, P.; Lin, Y.; Song, Q.; Gao, J. Supramolecular Assembly and Reversible Transition and of Chitosan Fluorescent Micelles by Noncovalent Modulation. *Advances in Polymer Technology* **2021**, *2021*, 1−10.
(53) Hu, X.; Yu, S.; Yang, G.; Long, W.; Guo, T.; Tian, J.; Liu, M.; Li, X.; Zhang, X.; Wei, Y. Fabrication of chitosan based luminescent nanoprobe with aggregation-induced emission feature through ultrasonic treatment. *Carbohydr. Polym.* **2022**, *291*, 119487.
(54) Marpu, S.; Upadhyay, P. K.; Nguyen, D. T.; Oswald, I. W.; Arvapally, R. K.; Petros, R. A.; Hu, Z.; Omary, M. A. Self-Assembly of Linear Polymers into Phosphorescent Nanoparticles: Optimization toward Non-Cytotoxic Bioimaging and Photonic Devices. *J. Phys. Chem. C* **2015**, *119*, 12551−12561.
(55) Alves, R.; Ravaro, L. P.; Pawlicka, A.; Silva, M. M.; de Camargo, A. S. Eco-friendly luminescent hybrid materials based on EuIII and LiI Co-doped chitosan. *J. Braz. Chem. Soc.* **2015**, *26*, 2590−2597.
(56) Begum, S.; Pandian, R.; Aswal, V. K.; Ramasamy, R. P. Chitosan−gold−lithium nanocomposites as solid polymer electrolyte. *J. Nanosci. Nanotechnol.* **2014**, *14*, 5761−5773.
(57) Salman, A.; Abdullah, O. G.; Hanna, R. R.; Aziz, S. B. Conductivity and Electrical Properties of Chitosan - Methylcellulose Blend Biopolymer Electrolyte Incorporated with Lithium Tetrafluoroborate. *Int. J. Electrochem. Sci.* **2018**, *13*, 3185−3199.
(58) Salleh, N.; Aziz, S. B.; Aspanut, Z.; Kadir, M. Electrical impedance and conduction mechanism analysis of biopolymer electrolytes based on methyl cellulose doped with ammonium iodide. *Ionics* **2016**, *22*, 2157−2167.
(59) Neese, F. Software update: the ORCA program system, version 4.0. *WIREs Computational Molecular Science* **2018**, *8*, e1327.
(60) Becke, A. D. Density-functional thermochemistry. III. The role of exact exchange. *J. Chem. Phys.* **1993**, *98*, 5648−5652.
(61) Lee, C.; Yang, W.; Parr, R. G. Development of the Colle-Salvetti correlation-energy formula into a functional of the electron density. *Phys. Rev. B* **1988**, *37*, 785−789.
(62) Weigend, F.; Ahlrichs, R. Balanced basis sets of split valence, triple zeta valence and quadruple zeta valence quality for H to Rn: Design and assessment of accuracy. *Phys. Chem. Chem. Phys.* **2005**, *7*, 3297−3305.
(63) Weigend, F. Accurate Coulomb-fitting basis sets for H to Rn. *Phys. Chem. Chem. Phys.* **2006**, *8*, 1057−1065.
(64) Grimme, S.; Antony, J.; Ehrlich, S.; Krieg, H. A consistent and accurate ab initio parametrization of density functional dispersion correction (DFT-D) for the 94 elements H-Pu. *J. Chem. Phys.* **2010**, *132*, 154104.
(65) Grimme, S.; Ehrlich, S.; Goerigk, L. Effect of the damping function in dispersion corrected density functional theory. *J. Comput. Chem.* **2011**, *32*, 1456−1465.
(66) Barone, V.; Cossi, M. Quantum Calculation of Molecular Energies and Energy Gradients in Solution by a Conductor Solvent Model. *J. Phys. Chem. A* **1998**, *102*, 1995−2001.
(67) Barak, P. Smoothing and differentiation by an adaptive-degree polynomial filter. *Anal. Chem.* **1995**, *67*, 2758−2762.
(68) Tauc, J.; Grigorovici, R.; Vancu, A. Optical properties and electronic structure of amorphous germanium. *physica status solidi (b)* **1966**, *15*, 627−637.
(69) Davis, E.; Mott, N. Conduction in non-crystalline systems V. Conductivity, optical absorption and photoconductivity in amorphous semiconductors. *Philosophical magazine* **1970**, *22*, 0903−0922.
(70) Mott, N. F.; Davis, E. A. *Electronic processes in non-crystalline materials*; Oxford university press, 2012.
(71) Osorio-Madrazo, A.; David, L.; Trombotto, S.; Lucas, J.-M.; Peniche-Covas, C.; Domard, A. Highly crystalline chitosan produced by multi-steps acid hydrolysis in the solid-state. *Carbohydr. Polym.* **2011**, *83*, 1730−1739.
(72) Alves, R.; De Camargo, A.; Pawlicka, A.; Silva, M. M. Luminescent polymer electrolytes based on chitosan and containing europium triflate. *Journal of Rare Earths* **2016**, *34*, 661−666.
(73) Sudaryanto; Yulianti, E.; Patimatuzzohrah. Structure and properties of solid polymer electrolyte based on chitosan and ZrO2 nanoparticle for lithium ion battery. *AIP Conference Proceedings* **2016**, *1710*, No. 020003.
(74) Aziz, S. B.; Abdullah, O. G.; Al-Zangana, S. Solid polymer electrolytes based on chitosan: NH4Tf modified by various amounts of TiO2 filler and its electrical and dielectric characteristics. *Int. J. Electrochem. Sci.* **2019**, *14*, 1909−1925.
(75) Morni, N.; Mohamed, N.; Arof, A. Silver nitrate doped chitosan acetate films and electrochemical cell performance. *Materials Science and Engineering: B* **1997**, *45*, 140−146.
(76) Morni, N.; Arof, A. Chitosan−lithium triflate electrolyte in secondary lithium cells. *J. Power Sources* **1999**, *77*, 42−48.
(77) Belamie, E.; Domard, A.; Chanzy, H.; Giraud-Guille, M.-M. Spherulitic crystallization of chitosan oligomers. *Langmuir* **1999**, *15*, 1549−1555.
(78) Mushi, N. E.; Utsel, S.; Berglund, L. A. Nanostructured biocomposite films of high toughness based on native chitin nanofibers and chitosan. *Front. Chem.* **2014**, *2*, 99.
(79) Silva, S. M.; Braga, C. R.; Fook, M. V.; Raposo, C. M.; Carvalho, L. H.; Canedo, E. L. In *Infrared Spectroscopy*, Theophanides, T., Ed.; IntechOpen: Rijeka, 2012; Chapter 2, pp 43−61.
(80) Fernandes Queiroz, M.; Melo, K. R. T.; Sabry, D. A.; Sassaki, G. L.; Rocha, H. A. O. Does the Use of Chitosan Contribute to Oxalate Kidney Stone Formation? *Marine Drugs* **2015**, *13*, 141−158.
(81) Knop, S.; Jansen, T. L. C.; Lindner, J.; Vohringer, P. On the nature of OH-stretching vibrations in hydrogen-bonded chains: Pump frequency dependent vibrational lifetime. *Phys. Chem. Chem. Phys.* **2011**, *13*, 4641−4650.
(82) Williams, P. C.; Norris, K. H.; Sobering, D. C. Determination of protein and moisture in wheat and barley by near-infrared transmission. *J. Agric. Food Chem.* **1985**, *33*, 239−244.
(83) Naumkin, A. V.; Kraut-Vass, A.; Gaarenstroom, S. W.; Powell, C. J. NIST X-ray Photoelectron Spectroscopy Database, *NIST Standard Reference Database Number 20*; 2000. DOI: 10.18434/T4T88K.
(84) Kowalczyk, S.; Ley, L.; McFeely, F.; Pollak, R.; Shirley, D. X-ray photoemission from sodium and lithium. *Phys. Rev. B* **1973**, *8*, 3583.

https://doi.org/10.1021/acsomega.2c08072
ACS Omega 2023, 8, 13763−13774

(85) Wood, K. N.; Teeter, G. XPS on Li-Battery-Related Compounds: Analysis of Inorganic SEI Phases and a Methodology for Charge Correction. *ACS Appl. Energy Mater.* **2018**, *1*, 4493−4504.
(86) Lin, L.; Liang, F.; Zhang, K.; Mao, H.; Yang, J.; Qian, Y. Lithium phosphide/lithium chloride coating on lithium for advanced lithium metal anode. *J. Mater. Chem. A* **2018**, *6*, 15859−15867.
(87) Escard, J.; Mavel, G.; Guerchais, J. E.; Kergoat, R. X-ray photoelectron spectroscopy study of some metal(II) halide and pseudohalide complexes. *Inorg. Chem.* **1974**, *13*, 695−701.
(88) Poinsignon, C. Polymer electrolytes. *Materials Science and Engineering: B* **1989**, *3*, 31−37.
(89) Niu, X.; Yang, X.; Mo, Z.; Guo, R.; Liu, N.; Zhao, P.; Liu, Z. Perylene-functionalized graphene sheets modified with *β*-cyclodextrin for the voltammetric discrimination of phenylalanine enantiomers. *Bioelectrochemistry* **2019**, *129*, 189−198.
(90) Moreno-Vásquez, M. J.; Valenzuela-Buitimea, E. L.; Plascencia-Jatomea, M.; Encinas- Encinas, J. C.; Rodríguez-Féelix, F.; Sánchez-Valdes, S.; Rosas-Burgos, E. C.; Ocaño- Higuera, V. M.; Graciano-Verdugo, A. Z. Functionalization of chitosan by a free radical reaction: Characterization, antioxidant and antibacterial potential. *Carbohydr. Polym.* **2017**, *155*, 117−127.
(91) Thirumuruganandham, S. P.; Cuevas Figueroa, J. L.; Baños, A. T.; Mowbray, D. J.; Terencio, T.; Martinez, M. O. Ab Initio Calculations of Chitosan Effects on the Electronic Properties of Unpassivated Triangular ZnO Nanowires Oriented along [0001] Directions. *ACS Omega* **2023**, *8*, 2337−2343.
(92) Yavuz, A. G.; Uygun, A.; Bhethanabotla, V. R. Substituted polyaniline/chitosan composites: Synthesis and characterization. *Carbohydr. Polym.* **2009**, *75*, 448−453.
(93) Kannusamy, P.; Sivalingam, T. Chitosan−ZnO/polyaniline hybrid composites: polymerization of aniline with chitosan−ZnO for better thermal and electrical property. *Polym. Degrad. Stab.* **2013**, *98*, 988−996.
(94) Hassan, M. A.; Omer, A. M.; Abbas, E.; Baset, W. M.; Tamer, T. M. Preparation, physicochemical characterization and antimicrobial activities of novel two phenolic chitosan Schiff base derivatives. *Sci. Rep.* **2018**, *8*, 1−14.
(95) Aziz, S. B. Morphological and optical characteristics of chitosan (1- x): Cuox ($4 \leq x \leq 12$) based polymer nano-composites: Optical dielectric loss as an alternative method for tauc's model. *Nanomaterials* **2017**, *7*, 444.
(96) Aziz, S. B.; Brza, M.; Nofal, M. M.; Abdulwahid, R. T.; Hussen, S. A.; Hussein, A. M.; Karim, W. O. A comprehensive review on optical properties of polymer electrolytes and composites. *Materials* **2020**, *13*, 3675.
(97) Paufler, P.; Elliott, S. R. *Physics of amorphous materials*; 1985.
(98) Yorkston, J.; Antonuk, L.; Morton, E.; Boudry, J.; Huang, V.; Kim, C.; Longo, M.; Street, R. The Dynamic Response of Htdrogenated Amorphous Silicon Imaging Pixels. *MRS Online Proceedings Library (OPL)* **1991**, *219*, 173.
(99) Mei, J.; Hong, Y.; Lam, J. W. Y.; Qin, A.; Tang, Y.; Tang, B. Z. Aggregation-Induced Emission: The Whole Is More Brilliant than the Parts. *Adv. Mater.* **2014**, *26*, 5429−5479.
(100) Gong, Y.; Tan, Y.; Mei, J.; Zhang, Y.; Yuan, W.; Zhang, Y.; Sun, J.; Tang, B. Z. Room temperature phosphorescence from natural products: Crystallization matters. *Science China Chemistry* **2013**, *56*, 1178−1182.
(101) Zhou, Q.; Liu, M.; Li, C.; Lu, S.; Jiang, J.; Yin, Y.; Zhang, Y.; Yang, L.; Shen, Y. Tunable photoluminescence properties of cotton fiber with gradually changing crystallinity. *Front. Chem.* **2022**, 632.

https://doi.org/10.1021/acsomega.2c08072
ACS Omega 2023, 8, 13763−13774